Cell Reports
Physical Science

CellPress
OPEN ACCESS

Article

Addressing solar photochemistry durability with an amorphous nickel antimonate photoanode

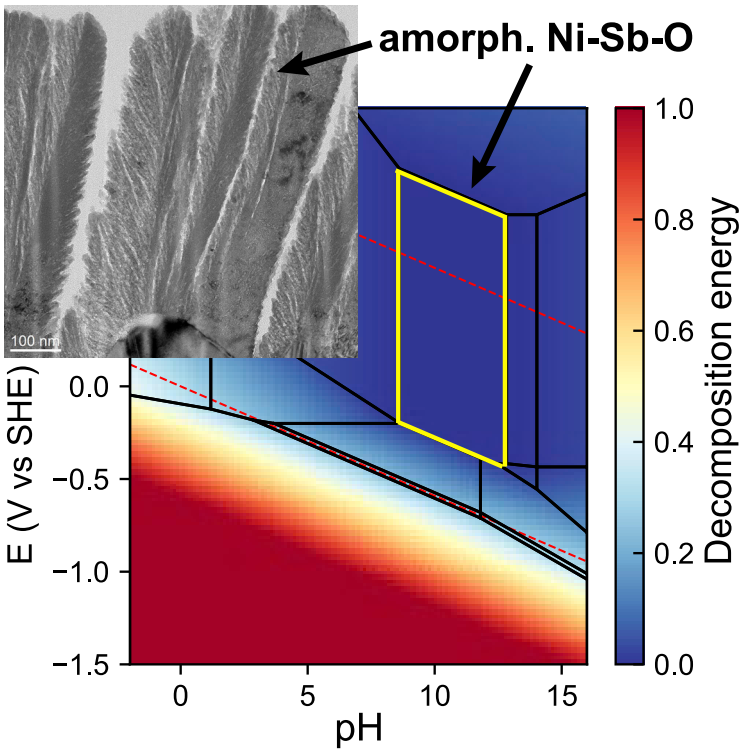

Harvesting solar energy to sustainably synthesize fuels requires the identification of materials that can operate durably for many years. Inspired by the corrosion resistance of amorphous oxides, Zhou et al. report an amorphous nickel antimonate with visible light photoactivity and lower corrosion than analogous materials, paving a pathway for further technology development.

Lan Zhou, Elizabeth A. Peterson, Karun K. Rao, ..., Jeffrey B. Neaton, Michal Bajdich, John M. Gregoire

gregoire@caltech.edu

Highlights

High-throughput experiments enable the discovery of an amorphous Ni-Sb photoanode

Favorable Pourbaix energetics and amorphous surface provide excellent durability

The broad spectral response stands in contrast to end members Sb_2O_5 and NiO

Electronic and chemical structure characterization pave the way for future study

Zhou et al., Cell Reports Physical Science 3, 100959
July 20, 2022
https://doi.org/10.1016/j.xcrp.2022.100959

Cell Reports
Physical Science

CellPress
OPEN ACCESS

Article

Addressing solar photochemistry durability with an amorphous nickel antimonate photoanode

Lan Zhou,[1,2] Elizabeth A. Peterson,[3,8] Karun K. Rao,[4,5] Yubing Lu,[6] Xiang Li,[7,8] Yungchieh Lai,[1,2] Sage R. Bauers,[9] Matthias H. Richter,[1,2] Kevin Kan,[1,2] Yu Wang,[1] Paul F. Newhouse,[1] Junko Yano,[6,8] Jeffrey B. Neaton,[3,8,10,11] Michal Bajdich,[4] and John M. Gregoire[1,2,12,*]

SUMMARY

Renewable generation of fuels using solar energy is a promising technology whose deployment hinges on the discovery of materials with a combination of durability and solar-to-chemical conversion efficiency that has yet to be demonstrated. Stable operation of photoanodes has been demonstrated with wide-gap semiconductors, as well as protected visible gap semiconductors. Visible photoresponse from electrochemically stable materials is quite rare. In this paper, we report the high-throughput discovery of an amorphous Ni-Sb (1:1) oxide photoanode that meets the requirements of operational stability, visible photoresponse, and appreciable photovoltage. X-ray absorption characterization of Ni and Sb establishes a structural connection to rutile $NiSb_2O_6$, guiding electronic structure characterization via X-ray photoelectron experiments and density functional theory. This amorphous photoanode opens avenues for photoelectrode development due to the lack of crystal anisotropy combined with its operational stability, which mitigates the formation of an interphase that disrupts the semiconductor-electrolyte junction.

INTRODUCTION

Solar photoelectrochemical (PEC) generation of chemical fuels using sunlight, H_2O, and CO_2 is a promising renewable energy technology whose technology readiness would be vastly improved by the identification of an efficient and robust photoanode for the oxygen evolution reaction (OER).[1,2] Multiphysics modeling has demonstrated that a variety of factors underlie the solar-to-chemical (STC) energy conversion efficiency, most centrally the band gaps of the 1, 2, or 3 absorbers.[3] The STC along with the cost of the source materials and the device durability are the central factors in determining the price of sustainably generated fuel, for which the US Department of Energy has established technology targets.[4] In this context, photoanode discovery research entails co-optimization concerning a breadth of performance criteria, including (1) operational PEC stability, (2) a band gap suitable for efficient utilization of the solar spectrum, (3) valence band energy (versus vacuum level) sufficiently negative to catalyze the OER, and (4) conduction band and Fermi energies sufficiently positive to perform the fuel-forming reaction or more commonly to couple to a photocathode in a tandem absorber configuration. Commensurate with these requirements are the energy conversion efficiency considerations of (5) maximizing external quantum efficiency (EQE), characterized as the fraction of incident photons that give rise to photoanodic current, and (6) maximizing photovoltage, which is typically characterized as minimizing the turn-on potential, i.e., the lowest potential

[1]Division of Engineering and Applied Science, California Institute of Technology, Pasadena, CA 91125, USA

[2]Liquid Sunlight Alliance, California Institute of Technology, Pasadena, CA 91125, USA

[3]Department of Physics, University of California, Berkeley, Berkeley, CA 94720, USA

[4]SUNCAT Center for Interface Science and Catalysis and Liquid Sunlight Alliance, SLAC National Accelerator Laboratory, Menlo Park, CA 94025, USA

[5]Department of Chemical Engineering, Stanford University, Stanford, CA 94305, USA

[6]Molecular Biophysics and Integrated Bioimaging Division, Lawrence Berkeley National Laboratory, Berkeley, CA 94720, USA

[7]SLAC National Accelerator Laboratory, Menlo Park, CA 94025, USA

[8]Liquid Sunlight Alliance, Lawrence Berkeley National Laboratory, Berkeley, CA 94720, USA

[9]Materials Science Center, National Renewable Energy Laboratory, Golden, CO 80401, USA

[10]Materials Sciences Division, Lawrence Berkeley National Laboratory, Berkeley, CA 94720, USA

[11]Kavli Energy NanoSciences Institute, University of California, Berkeley, Berkeley, CA 94720, USA

[12]Lead contact

*Correspondence: gregoire@caltech.edu

https://doi.org/10.1016/j.xcrp.2022.100959

at which anodic photocurrent is generated.[5–8] These efficiency considerations encompass the need for the photoanode to support the transport of photocarriers while mitigating carrier recombination. Regarding the chemical space of interest (7) earth-abundant elements are desirable for scalability of the resulting technology and (8) the metal elements (or more generally all elements other than O and H) and their equilibrium dissolved metals concentrations during operation must satisfy the requirements for device-level durability. We recently discussed this last requirement in the context of catalyst codesign.[9] For discovery research that is not constrained by a specific device architecture, requirements (1) and (8) correspond to the demonstration of a consistent photoactivity with low equilibrium dissolved metals concentrations, i.e., the dissolved metals concentrations at which the Pourbaix decomposition energy of the operational photoanode surface is zero. This last requirement alone limits the search space to metal oxides or semiconductors that form a metal oxide passivation layer. Many metal oxides also meet the band alignment and non-precious metal requirements, motivating the community's concerted effort to identify metal oxide phases that meet additional requirements. The recent proliferation in photoanode discovery has produced a compendium of metal oxides that each meet several but not all of these criteria.[10–12] Combinatorial synthesis and screening has been an effective strategy for discovering these photoanodes.[13–16] Hence the search continues with an increased focus on the two criteria that have been least commonly demonstrated: low turn-on potential and stable operation with low dissolved metals concentrations.

The majority of discovered visible light active phases (sub-2.8 eV band-gap energy) are V-, W-, and Fe-based oxide photoanodes, such as WO_3, α-Fe_2O_3, $BiVO_4$, several copper vanadates, $CuWO_4$, α-SnWO4, $FeWO_4$, and $BiFeO_3$.[5,6] Among these candidate photoanodes, performance limitations include insufficient utilization of the solar spectrum, poor charge carrier separation and transport, and poor operational stability. For example, WO_3 exhibits high operational stability in acidic electrolytes but suffers from a >2.7 eV band gap that substantially limits its solar conversion efficiency. Conversely, α-Fe_2O_3 shows a relatively low band-gap energy near 2 eV and high stability in alkaline media but is limited by its low carrier mobility and short hole diffusion length. A group of copper vanadates were identified with a 2 eV band gap and excellent stability in pH 9–10 electrolytes due to surface self-passivation but suffer from poor carrier transport and high turn-on potential.[17–22] $CuWO_4$ has a band gap between 2.2 and 2.4 eV and is stable under acidic and oxidizing conditions but exhibits poor photoactivity due to fast recombination of charge carriers, low electronic conductivity, and the presence of midgap electronic states on its surface.[23] Recent investigations of α-$SnWO_4$ have demonstrated favorable charge carrier transport properties and a suitable band gap of 1.9 eV, but the PEC performance could be limited by rapid surface passivation by SnO_2.[24,25] $BiVO_4$ is the most widely studied photoanode material, and the intensive effort to optimize its performance has resulted in nearly perfect carrier separation.[5] Its 2.4 eV band gap limits the STC efficiency[3] and its propensity for corrosion at all values of pH compromises device durability.[5]

The thermodynamic driving force toward corrosion is characterized by the Pourbaix decomposition energy, which is typically calculated at the concentration of a dissolved metal at or below 10^{-5} M.[26] A photoanode with an appreciable Pourbaix decomposition energy under operating conditions poses substantial challenges for attaining operational durability.[27] One strategy is to saturate the electrolyte with dissolved metals, as was recently demonstrated for $BiVO_4$ by using a high V^{5+} concentration to suppress corrosion.[28] We note in the discussion that this strategy

is often incompatible with device-level durability. Alternatively, the photoanode can "self-passivate" if a Pourbaix-stable phase forms on the surface to mitigate further corrosion. This interfacial layer plays a critical role in the photoanode efficiency, but its electronic properties cannot be rationally designed to optimize those properties because the chemistry and structure are dictated by corrosion processes. Identifying photoanodes with favorable Pourbaix decomposition energies is thus a promising avenue to overcome the hurdles in metal oxide photoanode performance, which we address in this work through combinatorial experiments akin to the theory-guided tiered screening workflow we reported previously.[11]

Metal antimonates, especially transition metal rutile structures of the form MSb_2O_6 (M = Mn, Co, Ni), have been studied for various applications, such as propane ammoxidation,[29] gas sensors,[30–32] lithium storage,[33] and visible light photocatalyst, for degradation of water pollutant.[34,35] More recently, using computational Pourbaix diagrams, these rutile antimonates were identified as Pourbaix-stable in potential ranges relevant for oxygen electrochemistry in strong acid electrolytes.[36,37] Several transition-metal antimonates have been investigated experimentally as electrocatalysts for OER,[38–41] the chlorine evolution reaction,[40,42] and oxygen reduction reaction.[43,44] This family of materials includes examples of visible light absorption, as well as activity and stability for OER, motivating our combinatorial investigation of Ni-Sb oxide library as visible light photoanodes, which, to the best of our knowledge, has not been previously reported. While we successfully synthesized one target phase, $NiSb_2O_6$, its underwhelming photoactivity hinders its further development as a photoanode, despite its favorable Pourbaix energetics. By virtue of the combinatorial nature of our experiments, we identified a more promising material that exhibits similarities to $NiSb_2O_6$ but has a Ni:Sb ratio near 1 and is amorphous. This photoanode is referred to herein as am-$NiSbO_z$ and its appreciable EQE, despite its lack of crystallinity, is unique among known photoanodes. Our combined experiment and theory characterization of this material demonstrates that it performs quite well concerning the requirements for broad spectral response, operational stability, and turn-on potential.

RESULTS

High-throughput experimentation

Combinatorial exploration of the Ni-Sb oxide system commenced with the synthesis of a Ni_xSb_{1-x} oxide composition spread thin film on F-doped SnO_2 (FTO)/Tec7 glass substrate, which was subsequently annealed at 610°C in air. A series of compositions were characterized for photoactivity in a three-electrode scanning drop cell (SDC) (Figure 1A) using toggled illumination chronoamperometry (CA) at 1.23 V versus RHE at 12 combinations of electrolyte and photon energy. A new series of as-synthesized compositions were used for each of the three electrolytes, which included pH 10 and pH 7 electrolytes with 0.01 M sodium sulfite (SLF) as well as pH 1 electrolyte with 0.1 M methanol (MET), as shown in Table S1. Each composition in each electrolyte was measured under 3.2, 2.7, 2.4, and 2.06 eV illumination (Figure 1B). Sulfite and methanol served as sacrificial hole acceptors to characterize photoactivity without requiring the photoanode surfaces to support the OER. The results are summarized in Figure 1C using the EQE (Note S1) to adjust the measured photocurrent by the different illumination intensities (Tables S2 and S3). While all Ni_xSb_{1-x} oxide compositions exhibited photo activity in at least one of these 12 conditions, the compositions with $x < 0.35$ were only photoactive under 2.7 and 3.2 eV illumination. More Ni-rich compositions exhibited photoactivity at low photon energies with substantial sensitivity to composition, especially at pH 10, where increasing the nickel

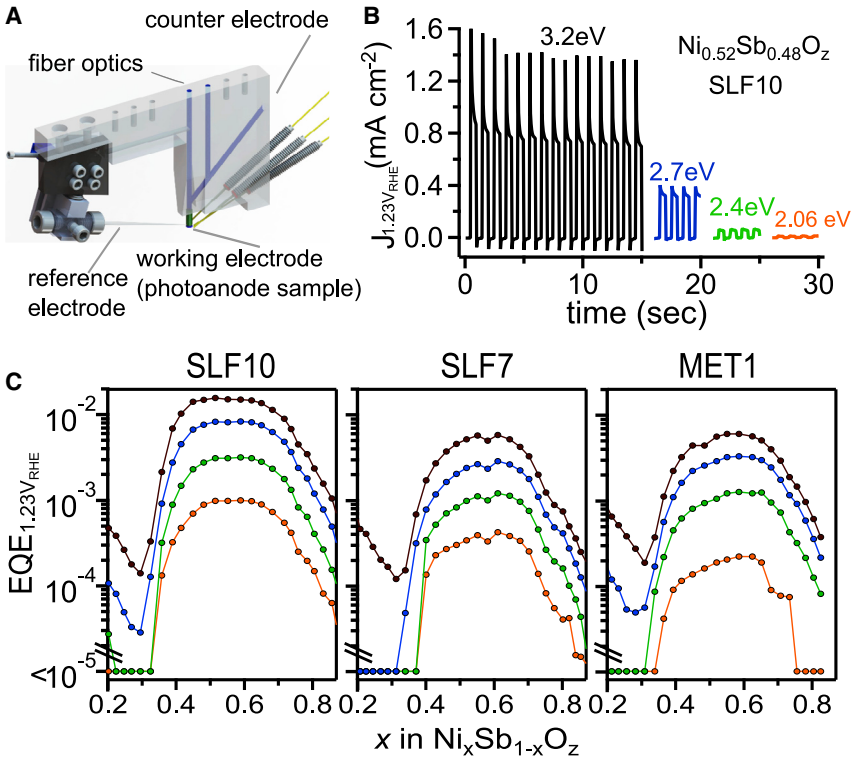

Figure 1. Combinatorial photoelectrochemical characterization of Ni-Sb oxides

(A) Schematic of the scanning droplet cell used in the combinatorial photoelectrochemical measurements.

(B) Photocurrent density under four illumination sources at the applied potential of 1.23 V versus RHE for each photoanode thin film sample in the Ni-Sb oxide library in the pH 10 electrolyte with 0.01 M sodium sulfite (SLF10), as shown here for sample $Ni_{0.52}Sb_{0.48}O_z$.

(C) The resulting EQE values calculated from photocurrent density for each illumination source in SLF10, sulfite-containing pH 7 (SLF7), and methanol-containing pH 1 (MET1) electrolytes shown as a function of Ni composition, x. The corresponding LED energies are indicated by colors shown in (B): black, blue, green, and orange refer to photon energies of 3.2, 2.7, 2.4, and 2.06 eV, respectively.

concentration from $x = 0.35$ to 0.5 resulted in a nearly 10-fold increase in EQE. With increasing x above 0.5, the EQE decreases slowly and then more dramatically, enabling the identification of the $x = 0.5$ composition as a primary target for further characterization as well as the $x = 0.33$ composition as a valuable point of comparison.

The selection of these compositions of interest is further supported by the phase behavior of the oxide composition spread. X-ray diffraction (XRD) measurements in Figure 2 revealed the presence of two crystalline phases. The rutile $NiSb_2O_6$ structure exhibits appreciable intensity for $x \leq 0.33$, the formula unit value, with decreasing intensity as x increases such that the signal is near the detectability limit at $x = 0.5$. When x increases above 0.7 a weak NiO signal is observed with intensity increasing as x increases. Collectively the results indicate that the film contains an X-ray amorphous component for all compositions with $x > 0.33$, which corresponds to all compositions where photoactivity at 2.06 or 2.4 eV illumination was observed (Figure 1C). This X-ray amorphous phase is in high phase purity from $x = 0.5$ to 0.6, which corresponds to the compositions where the highest photoactivity was observed for each photon energy. In our experience with metal oxide deposition, many compositions are X-ray amorphous as-deposited, but only the most refractory

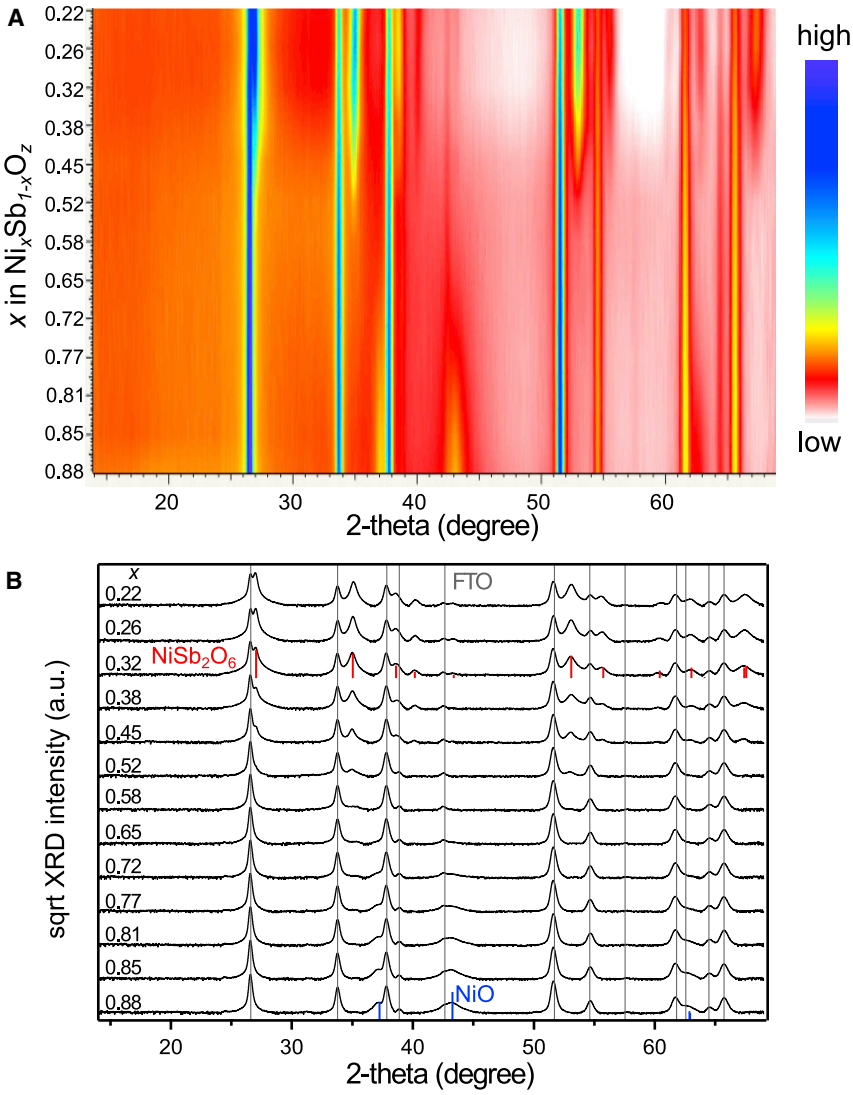

Figure 2. Structural and phase distribution characterization of the Ni-Sb oxide library

(A) XRD intensity heatmap of as-synthesized $Ni_xSb_{1-x}O_z$ binary composition spread annealed at 610°C with Ni concentration x from 0.22 to 0.88 without background subtraction, where the FTO substrate contributes to the peaks that are observed at all compositions. The increased intensity of the broad features with 2-theta < 40° for $x > 0.38$ is consistent with scattering from an amorphous phase.

(B) The corresponding XRD intensity curves after background subtraction. Below Ni concentration of 0.32, all the diffraction peaks besides ones from FTO substrates (ICDD no. 01-070-6153) are in good agreement with the rutile structure of $NiSb_2O_6$ (tetragonal with space group of $P4_2/mnm$, and lattice constants of a = 4.662 Å and c = 3.068 Å. The red stick patterns were modified using rutile $MnSb_2O_6$ phase with ICDD no. 04-011-4962). With increasing Ni concentration x, rutile $NiSb_2O_6$ intensity drops, resulting in an X-ray amorphous composition region between x = 0.52–0.65, and NiO (blue sticks, ICDD no. 00-044-1159) appears in the thin film while Ni concentration $x > 0.72$.

oxides resist crystallization upon annealing at 610°C. We have not found literature characterization of amorphous oxides in this composition region and herein refer to this phase as am-$NiSbO_z$.

Computational and experimental assessment of durability

While the lack of a structural model for am-$NiSbO_z$ limits the ability to computationally characterize its formation energy, we estimate the energetics of this

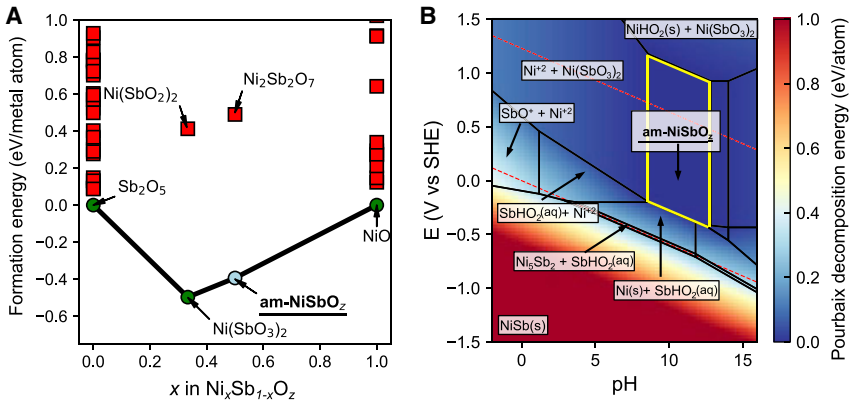

Figure 3. Grand potential phase diagram and Pourbaix stability analysis of Ni-Sb oxide system

(A) Calculated formation energy variation with the Ni concentration under the chemical potential of oxygen $\mu_{O2} = -5.9$ eV to approximate synthesis conditions. All phases above-hull are labeled with red squares, while the on-hull tri-rutile $NiSb_2O_6$ and two end oxides Sb_2O_5 and NiO are indicated with green circles. The experimentally observed phase am-$NiSbO_z$ (blue circle at $x = 0.5$) is considered to exist on the tie line between $NiSb_2O_6$ and NiO.

(B) Computationally predicted Pourbaix diagram of Ni-Sb-O using MP data augmented with the am-$NiSbO_z$ phase. The ion concentration for metal is fixed at 10^{-6} M. The Gibbs free energy of am-$NiSbO_z$ decomposition with respect to the Pourbaix-stable phases is superimposed as a heatmap on the diagram. The thermodynamic stability window of am-$NiSbO_z$ (yellow outline) extends from approximately 0.2 to 1.7 V versus RHE and from pH 9 to 13. The two red dashed lines denote 0 and 1.23 V versus RHE, respectively.

phase by first calculating the Ni-Sb-O grand potential phase diagram (Figure 3A). Using an oxygen chemical potential of −5.9 eV (½ O_2 from Materials Project [MP] plus −1 eV correction for experimental synthesis conditions relative to standard conditions) and considering all phases in the MP, the only stable ternary oxide phase occurs at a Ni composition of 0.33 ($NiSb_2O_6$, mp-505271). At the composition $x = 0.5$, a pyrochlore phase $Ni_2Sb_2O_7$ (mp-1190650) appears at 0.88 eV per metal atom above the solid-state free energy hull. This phase has been synthesized[45] but is not observed in this work. Since the exact formation energy of am-$NiSbO_z$ is unknown, we approximate that this phase lies on the free energy hull on the coexistence line between $NiSb_2O_6$ and NiO (Figure 3A), which is likely the lower limit of the true formation energy and serves as a non-arbitrary way to place this phase on the phase diagram. Under this approximation, the Pourbaix energetics of am-$NiSbO_z$ can be evaluated using the MP Pourbaix module, resulting in the Pourbaix diagram and corresponding map of Pourbaix decomposition energy (G_{pbx}) in Figure 3B. These bulk thermodynamics indicate that am-$NiSbO_z$ may self-passivate with a $NiSb_2O_6$ layer in neutral to acidic OER conditions. In pH 10 electrolyte, am-$NiSbO_z$ is thermodynamically stable under OER conditions. The Pourbaix diagram of $NiSb_2O_6$ is qualitatively similar (Figure S1, Note S2), especially under mild alkaline conditions. We note that, if the true formation energy of am-$NiSbO_z$ corresponds to the above-hull energy in Figure 3A, the minimum G_{pbx} of am-$NiSbO_z$ in Figure 3B would become this same above-hull energy due to the thermodynamic preference for decomposing into $NiSb_2O_6$ and NiO, although for OER-relevant potentials in pH 10 the predicted lack of corrosion would remain unchanged.

At lower potentials, am-$NiSbO_z$ and $NiSb_2O_6$ are predicted to undergo cathodic corrosion at potentials of 0.5, 0.35, and 0.3 V versus RHE for pH 1, 7, and 10, respectively (Figure 3B). This prediction is consistent with the experimental observation of

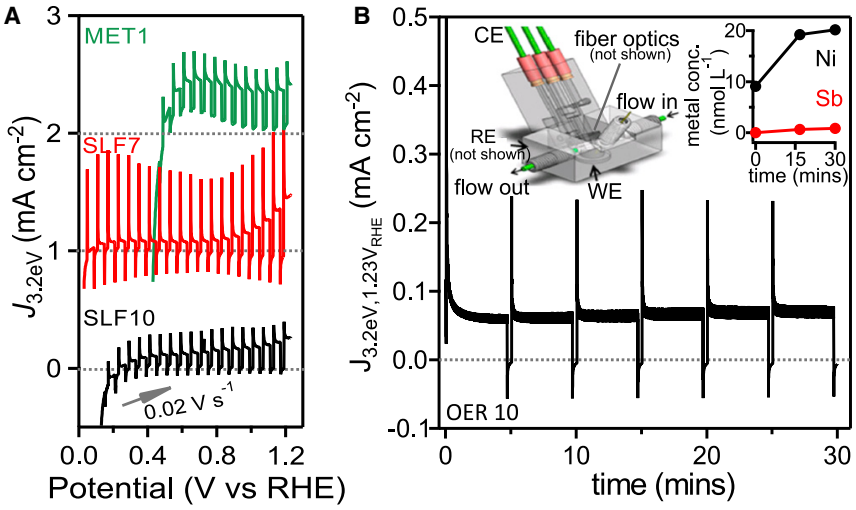

Figure 4. Photoactivity and photostability characterization of am-NiSbO$_z$

(A) The anodic sweep of CV measurements under toggled 3.2 eV illumination in pH 1, 7, and 10 electrolytes containing hole acceptors, each acquired on $x = 0.5$ electrodes that have only been operated in the respective electrolyte.

(B) A 30 min CA under 3.2 eV illumination at the applied potential of 1.23 V versus RHE measured on a 0.312 cm^2 electrode in a recirculating flow cell containing 74 mL O_2-bubbled pH 10 electrolyte without a hole acceptor. Inset: schematic of the flow cell (left) and dissolved metals concentrations measured by ICP-MS of electrolyte from three aliquots (right).

dark cathodic current for potentials below 0.4, 0.1, and 0.2 V versus RHE for pH 1, 7, and 10, respectively, as revealed by toggled illumination voltage sweeps under 3.2 eV illumination (Figure S2). The final anodic sweep for each electrolyte is shown in Figure 4A. While a dark cathodic current obscures the observation of the turn-on potential for anodic photocurrent, the pH 7 electrolyte offers the largest potential window without substantial dark current, where the turn-on potential is near or below 0.1 V versus RHE (Figure 4A). In pH 10, where the highest EQE was observed in Figure 1C, the photocurrent versus potential is mostly convex in the potential region with near-zero dark current (Figure 4A), suggesting a fill factor in excess of 0.5, which is promising for a photoanode that has yet to undergo optimization. The substantial current transients upon illumination toggling illumination indicate the persistence of surface recombination despite the use of a sacrificial hole acceptor, suggesting that further improvements in photoactivity may be achieved with optimized surface treatments.

Additional characterization of photoanode stability in this electrolyte (pH 10) was performed in an electrochemical recirculation flow cell (Figure 4B, insert) with a bipolar membrane separating the anolyte and catholyte to enable the photoanode to equilibrate with dissolved metals concentrations in the electrolyte. The corresponding results (Figure 4B) demonstrate substantial photoanodic current at 1.23 V versus RHE throughout the 30-min measurement with near-zero dark current measured every 5 min. Inductively coupled plasma mass spectroscopy (ICP-MS) analysis of three-electrolyte aliquots from this experiment shows a very low Sb concentration on the order of 1 nmol L^{-1}, with a larger, but still low Ni concentration, which increases from approximately 9 to 20 nmol L^{-1} throughout the measurement. These results are consistent with the computed Pourbaix diagram (Figure 3B), which indicates that critical dissolved metals concentrations for the onset of corrosion are below 1 μmol L^{-1}.

After an initial transient in photocurrent, the slowly increasing photocurrent over the duration of the measurement coincides with a continually increasing dissolved Ni concentration. To ensure that photostability was not contingent on the presence of a sacrificial hole acceptor, this measurement was done without SLF. We note that the average Ni corrosion rate of 0.37 nmol L^{-1} min^{-1} corresponds to an anodic corrosion current density of $n \times 1.4 \times 10^{-4}$ mA cm^{-2} assuming an anodic corrosion process with n e^- per corroded Ni atom. This corrosion accounts for $n \times 0.2\%$ of the anodic charge passed during the experiment. Under OER conditions, Ni^{2+} is the presumed aqueous species, which implicates a corrosion reaction with $n = 2$, e.g., $NiO \rightarrow Ni^{2+} + 2\,e^- + 0.5\,O_2$. We ignore the contribution of Sb corrosion to the current density since its dissolved metals concentration is more than 10× lower than that of Ni. Assuming that the only anodic process other than corrosion is the OER, the corresponding OER Faradaic efficiency is 99.6%.

Given that corrosion is an insignificant contributor to the photocurrent in Figure 4B, the two most likely explanations for the rise in photocurrent over the 30-min measurement are a continued exchange of surface and dissolved Ni that increases OER activity compared with the initial surface, or improved carrier extraction due to the formation of a Sb-rich surface layer. The near-surface Ni composition was measured by X-ray photoelectron spectroscopy (XPS) (Figures S3 and S4) to be $x = 0.46$ after operation, which is commensurate with the Ni corrosion being higher than Sb and corresponds to a solid-state Sb enrichment by 4.3 nmol cm^{-2}. The corresponding thickness of a passivation layer with composition $x = 0.46$ compared with the bulk value of $x = 0.5$ is 8.8 nm. If the passivation layer was Ni-free, i.e., similar to Sb_2O_5, the thickness corresponding to the differential corrosion would be 3.7 nm. These nominal passivation layer thicknesses assume a planar thin film, and the increase in specific surface area from any non-planar structure would correspond to a proportional decrease in the passivation layer thickness. For example, with a roughness factor of 10, the passivation layer may be as thin as 0.37 nm. Figure 1 shows lower EQE at pH 1 and pH 7, coinciding with the indication from the Pourbaix diagram of Figure 3B that a greater extent of Ni corrosion will be required to enable passivation by $NiSb_2O_6$. The passivation layer thickness is likely thicker under those conditions, which may underlie the decrease in photoactivity.

Structural and electronic characterization

Continued characterization of the am-$NiSbO_z$ photoanode proceeded with transmission electron microscopy (TEM). Cross-section TEM images are shown in Figures 5A and 5B for am-$NiSbO_z$ samples, one in the as-synthesized condition as well as the sample that underwent the 30-min stability test in Figure 4B. The films exhibit an angled columnar structure that likely arises from the off-axis deposition in the combinatorial synthesis. A comparison of these images with the corresponding elemental maps (Figure S5) reveals that the majority of each film has x near 0.5, while the columnar growth appears to have caused some lateral composition inhomogeneity due to shadowing of the depositing flux of Ni and Sb, whose deposition sources were located on opposing sides of the substrate to achieve the desired composition spread. The Sb-rich regions have a distinct appearance in the images of Figures 5A and 5B, motivating selected area electron diffraction (SAED) characterization of these regions as well as a region that represents the majority of the film. The results in Figures 5C and 5D demonstrate that the Sb-rich minority regions contain crystalline $NiSb_2O_6$, while the majority region has no discernable crystallinity (Figure S6), in excellent agreement with the XRD analysis of Figure 2 where the persistence of a small $NiSb_2O_6$ signal up to $x = 0.5$ is due to small crystallites on the sides of the pillars facing the Sb deposition source. Given that the $NiSb_2O_6$

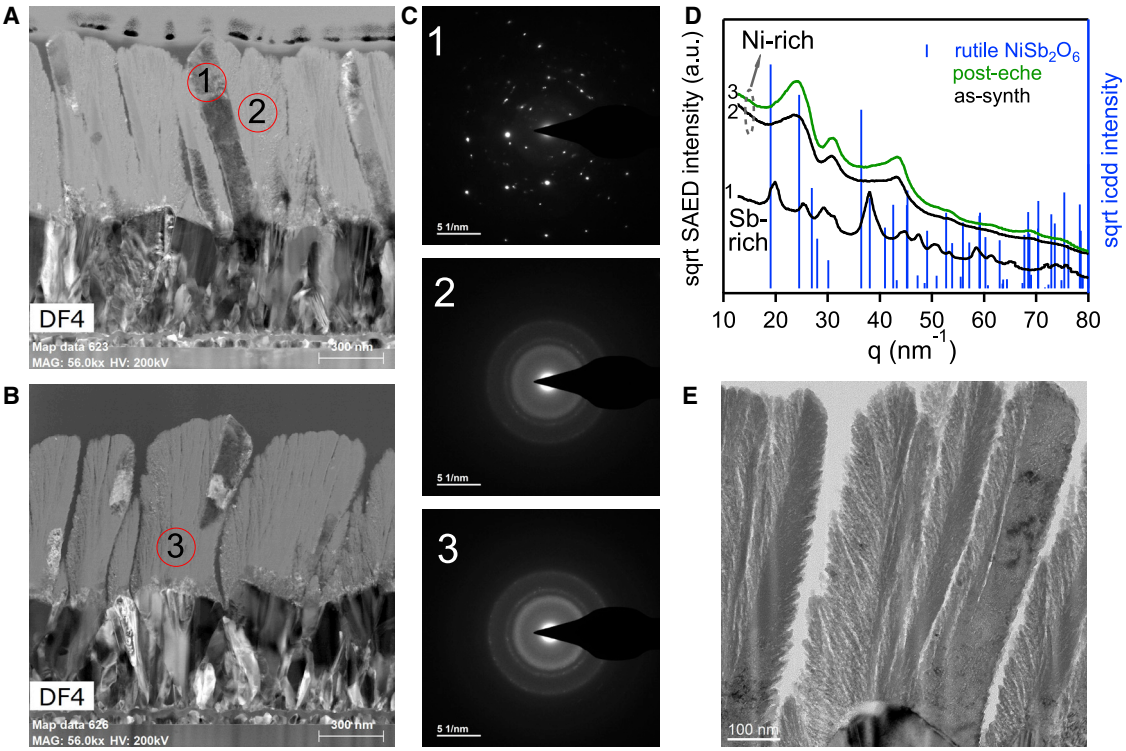

Figure 5. Structural and morphological characterization of am-$NiSbO_z$

(A and B) TEM cross-section images of (A) as-synthesized and (B) post-PEC (pH 10) am-$NiSbO_z$ photoanodes. Both samples exhibit an angled columnar growth with different, arbitrary orientations of the ion-milled cross-sections.

(C) The selected area electron diffraction (SAED) images from the regions are indicated by the red circles in (A and B). Region 1 is Sb-rich while regions 2 and 3 are slightly Ni-rich compared with the average film composition of $x = 0.5$, as indicated by EDX elemental mapping shown in Figure S5.

(D) The integrated SAED intensity spectra as a function of q, the scattering vector, along with the rutile $NiSb_2O_6$ ICDD stick patterns in blue, showing that the Sb-rich portion of the film contains this rutile structure, while the other spots have no detected crystallinity.

(E) A high-resolution TEM image showing the sub-10-nm feather-like morphology with the columnar structure.

sample at $x = 0.33$ has low photoactivity compared with the $x = 0.5$ region, we continue to conclude that the photoactivity arises primarily from the amorphous (am-$NiSbO_z$) material (ignoring any heterojunction effects). The elemental mapping by energy-dispersive X-ray spectroscopy (EDX) in TEM (Figure S5) indicates that the oxygen stoichiometry z is approximately 3.4, which is similar to the value of 3.5 corresponding to the above modeling of this amorphous phase as being in equilibrium with a combination of $NiSb_2O_6$ and NiO.

The higher-resolution image in Figure 5E reveals a feather-like nanostructure. We are not aware of a previous observation of such a morphology in an amorphous film. To confirm that the overall phase behavior and photoactivity are not produced by the lateral composition homogeneities, we synthesized and characterized an $x = 0.5$ film deposited and annealed using the same conditions but with a Pt/Ti/SiO_2/Si substrate, which has much lower surface roughness than the F-doped SnO_2/glass substrate. The results are shown in Figure S7 and support the existence of a nanostructured, amorphous am-$NiSbO_z$ photoanode with a broad spectral response.

To characterize the charge carrier dynamics of the photoanode, we proceeded with Hall effect measurements of the $x = 0.33$ and $x = 0.5$ samples. The 300-nm-thick films of these compositions were deposited on SiO_2/Si wafers and post-annealed at

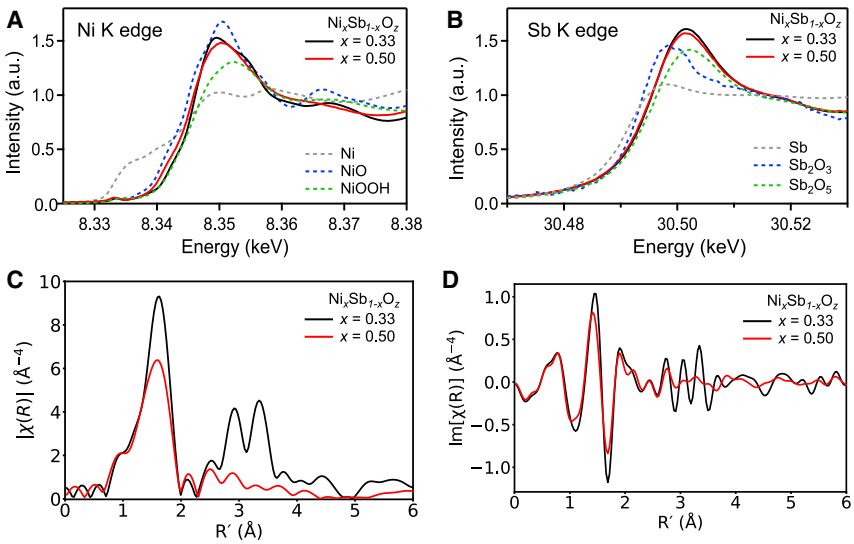

Figure 6. XAS analysis of Ni-Sb oxides

(A and B) (A) Ni and (B) Sb K-edge XAS spectra of as-synthesized $Ni_xSb_{1-x}O_z$ photoanodes at Ni concentration of $x = 0.33$ ($NiSb_2O_6$) and 0.5 (am-$NiSbO_z$). The binary oxide references are shown in dashed lines.

(C and D) Ni K-edge Fourier transformed XAS spectra in (C) R-space magnitude and (D) R-space imaginary part.

610°C, then cleaved into 1 × 1 cm samples with evaporated Au/Ti metal contacts. The resistivity of the $x = 0.33$ sample was measured to be 0.57 ± 0.01 Ω-cm and from the negative Hall voltage we determined an electron mobility of approximately 0.09 ± 0.01 $cm^2 V^{-1} s^{-1}$. The $x = 0.5$ sample exhibited a resistance above 100 MΩ, which prohibited reliable characterization of the resistivity or mobility. Low mobilities of only ca. 0.2 $cm^2 V^{-1} s^{-1}$ have been measured in other high-performing oxide photoanodes, such as $BiVO_4$, which is attributed to polaron formation.[46] Whether either the 0.33 or 0.5 compositions can meet or surpass such values with improvements in microstructure and density remains to be seen. In particular, the TEM analysis of Figures 5 and S5 indicates a high density of columnar voids that preclude lateral or in-plane conduction. While the deposition of $x = 0.5$ on a flatter substrate exhibits less nanostructure (Figure S7), columnar voids are still present. As a result, this morphology is likely inflating the measured resistance compared with the intrinsic resistivity of the material, motivating future deposition of compact films to facilitate electronic characterization.

To characterize the relationship between am-$NiSbO_z$ and $NiSb_2O_6$, we conducted X-ray absorption near-edge spectroscopy (XANES), as shown in Figures 6A and 6B, where the signals from the Sb K-edge are nearly identical with edge positions matching that of Sb_2O_5. The signals from the Ni K-edge are similar for these two samples with edge positions between those of the NiO and NiOOH reference materials. The $x = 0.33$ ($NiSb_2O_6$) sample exhibits a higher edge energy, suggesting that the Ni is slightly more oxidized in this material. The high-resolution core-level Ni $2p_{3/2}$ XPS spectra of the same two samples in Figure S4 are also quite similar. Both spectra are well modeled by a pair of Ni species with Ni $2p_{3/2}$ binding energies of 856.0 and 857.2 eV, which are characteristic of $Ni^{2+}(OH)_2$ and $Ni^{3+}OOH$, respectively. The Ni^{2+}/Ni^{3+} ratios directly calculated from the area under each spectrum peak are 1.07 and 1.43, respectively, for the $x = 0.5$ and 0.33 samples, indicating that am-$NiSbO_z$ is more oxidized than $NiSb_2O_6$ on the surface (after air exposure)

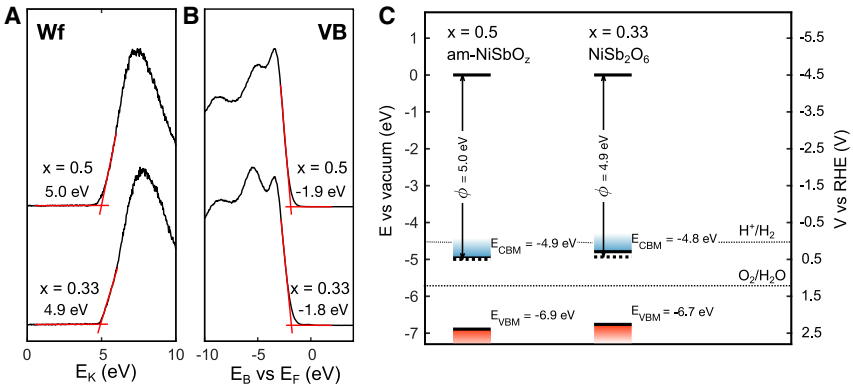

Figure 7. Band energetics characterization of Ni-Sb oxides

(A and B) XPS characterization of the (A) work function and (B) valence band are shown for as-synthesized $x = 0.5$ (am-$NiSbO_z$) and $x = 0.33$ ($NiSb_2O_6$) films. The respective energies are labeled according to the onset of the XPS signal as modeled by the linear segments (red).

(C) The band energetics of each material relative to the vacuum level are shown using the modeled work function from (A) for the Fermi energy (black dashed lines) and the valence band position below the Fermi energy taken from (B). The conduction band for each material is drawn at 2 eV above the valence band, an approximation based on optical absorption and the photon energy of photocurrent onset. The water redox potentials of H^+/H_2 (0 V versus RHE) and O_2/H_2O (1.23 V versus RHE) are indicated as dashed lines.

even though the X-ray absorption spectroscopy (XAS) data suggest that the bulk Ni is more oxidized in the $NiSb_2O_6$ sample.

To characterize the environments around Ni for am-$NiSbO_z$ and $NiSb_2O_6$, we obtained Ni-K extended X-ray absorption fine structure (EXAFS) signals. The fitting of the first shell in the EXAFS signal (Figures S8 and S9) was performed using the Ni-O scattering path templated by the computational $NiSb_2O_6$ structure (mp-505271). The fitted parameters (Table S4) include similar Ni-O distances of 2.02 ± 0.01 and 2.04 ± 0.01 am-$NiSbO_z$ and $NiSb_2O_6$, respectively. The corresponding coordination numbers (CN) are 5.02 ± 0.72 and 5.53 ± 0.30, respectively. The higher CN for $x = 0.33$ ($NiSb_2O_6$) is consistent with a higher oxidation state inferred from the XANES edge position, although the fitted CN values are within the uncertainty. The $x = 0.5$ sample exhibits weak signals from higher-order scattering paths, which is consistent with its amorphous structure. The stronger signal from the crystalline $x = 0.33$ sample enabled multi-shell fitting, which corroborated the XRD and TEM identification of the $NiSb_2O_6$ structure (Figure S10; Table S4; Note S3). Collectively, the results demonstrate similar Ni-O environments for these two materials with the characterization of a higher-order coordination environment of am-$NiSbO_z$ obscured by its amorphous structure.

To characterize the band energetics of am-$NiSbO_z$ and $NiSb_2O_6$, as-synthesized samples were characterized via XPS where each valence band position with respect to vacuum and work function were determined from the onset of XPS intensity at low and high binding energy, respectively. The results shown in Figure 7 indicate similar valence band energies and Fermi levels for each of these semiconductors, with the Fermi energy residing approximately 2 eV above the valence band maximum (VBM) and band edges compared with the redox potential (versus RHE) of the water-splitting reaction suitable for a photoanode in a tandem absorber solar fuel generator. The conduction band minimum (CBM) of am-$NiSbO_z$ is around -4.9 eV at vacuum level (0.4 V versus RHE), indicating that the maximum photovoltage that can be achieved by am-$NiSbO_z$ is around 1.23–0.4 = 0.83 V. This is in excellent agreement with the photovoltage gain obtained from the sulfite oxidation PEC measurements

(Figures 4A and S2). The turn-on potential of am-$NiSbO_z$ is observed below 0.4 V versus RHE, corresponding to the photovoltage in excess of 1.23–0.4 = 0.83 V. For am-$NiSbO_z$, photoactivity was observed with 2.1 eV illumination, or more specifically with a light-emitting diode (LED) with center and line-width of 2.06 $\pm$ 0.03 eV. A band-gap energy no larger than this energy, especially considering the possibility of an increased optical band gap compared with the electronic band gap due to the exciton binding energy, would place the Fermi level very close to the CBM. Optical characterization (Figure S11) of the am-$NiSbO_z$ and $NiSb_2O_6$ samples also reveals very similar spectral absorption. The Tauc plots to characterize direct-allowed and indirect-allowed optical transitions do not exhibit a region with a strong linear relationship with photon energy, compromising the precise determination of the band-gap energy from the optical data. The Tauc plot for indirect band gaps contains the most linear region above 2.5 eV and supports the existence of an indirect band gap. While the indirect Tauc plot is consistent with a 2-eV band gap, the band-gap energy is better characterized by the photocurrent onset and XPS results, which indicate that the band-gap energy of both am-$NiSbO_z$ and $NiSb_2O_6$ is 2 eV with an uncertainty approximated to be $\pm$0.1 eV based on the lower bound from XPS and upper bound from photon energy onset. Previous experimental characterization of the band gap of $NiSb_2O_6$ ranges from 1.6[35] to 2.83 eV.[34] While the am-$NiSbO_z$ shows substantially higher EQE than the $NiSb_2O_6$ photoanode, it is worth noting that the optical absorptivity of am-$NiSbO_z$ is approximately 1.5× lower over the entire visible range (1.5–3.0 eV). The increasing photoactivity with increasing Ni is not explained by optical absorption, which is contrary to the general behavior that the high defect density of amorphous materials contributes to substantial optical absorption.

To further characterize the electronic structure of am-$NiSbO_z$, we consider the connection to $Ni_2Sb_2O_7$, which has approximately the same cation composition as the samples with the highest EQE in Figure 1C, and the connection to $NiSb_2O_6$ established by the XAS and band energetics experiments (Figures 6 and 7). For each of these crystalline structures, we performed density functional theory (DFT) calculations using the Vienna Ab initio Simulation Package (VASP)[47,48] with Hubbard U corrections[49,50] applied to the Ni d-states, revealing sensitivities with respect to the band-gap and formation energies (Figures S12 and S13). Both ferromagnetic (FM) and antiferromagnetic (AFM) configurations of spins centered on the Ni sites were considered. In particular, AFM orderings were found to be more stable than the FM ordering by 213 meV per metal atom for $NiSb_2O_6$ and by 636 meV per metal cation for $Ni_2Sb_2O_7$. For $NiSb_2O_6$, both FM and AFM orderings had very similar lattice parameters and adopted a tetragonal crystal structure. For $Ni_2Sb_2O_7$, however, the FM ordering corresponded to a cubic structure, while the AFM ordering produces a small tetragonal distortion with two of the lattice parameters expanding by 0.36% and the third contracting by 0.33%. Given the default MP FM ordering used for Figure 3, this strong magnetic-ordering dependence of $Ni_2Sb_2O_7$ formation energy indicates that its above-hull energy in Figure 3A may be over-estimated. Furthermore, $Ni_2Sb_2O_7$ with FM ordering was found to be metallic in our DFT+U calculations, underscoring the importance of carefully considering magnetism in these materials (Table S5). The element projected density of states of $NiSb_2O_6$ calculated with DFT-PBE+U (Figure 8A) leads to a band gap of 1.03 eV, a valence band of predominantly oxygen character, and a conduction band with a very low density of states of predominantly antimony character.

To improve the treatment of short-range exchange and correlation effects and ascertain the associated sensitivity toward the electronic structure, $NiSb_2O_6$ in the AFM state was also evaluated using the hybrid functional of Heyd, Scuseria, and Ernzerhof

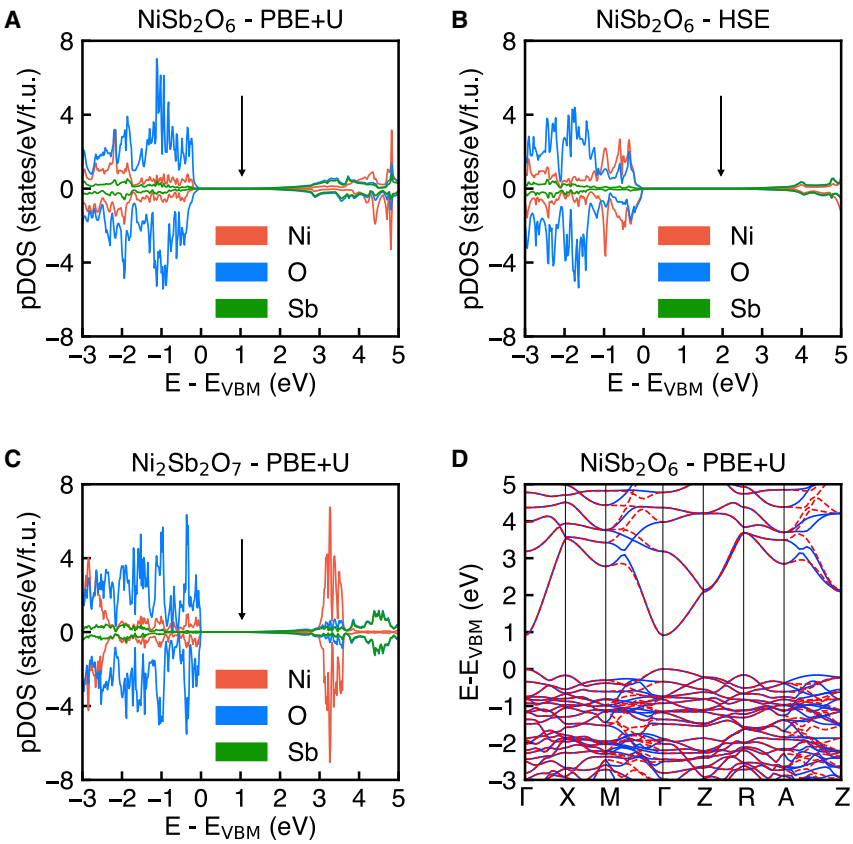

Figure 8. Electronic structure of Ni-Sb oxides

(A) Element projected density of states of $NiSb_2O_6$ calculated with DFT-PBE+U.

(B) Element projected density of states of $NiSb_2O_6$ calculated with DFT-HSE06.

(C) Projected density of states (PDOS) of $Ni_2Sb_2O_7$ calculated with PBE+U. The arrows in (A–C) indicate the conduction band minimum.

(D) Band structure of $NiSb_2O_6$ calculated with PBE+U, which corresponds to the density of states in (A). Solid blue lines and red dashed lines represent the up and down spin channels. The conduction bands are highly dispersive, which accounts for the diminished density of states at the conduction band edges of plots (A–C). Both $NiSb_2O_6$ and $Ni_2Sb_2O_7$ have a DFT-PBE+U band gap near 1 eV, and $NiSb_2O_6$ has a DFT-HSE06 band gap near 2 eV. All calculations used an antiferromagnetic magnetic ordering.

(HSE06),[51,52] which can provide an improved description of band gaps and electronic structure. The resulting density of states (Figure 8B) has a larger band gap of 1.96 eV that well matches the experimental results of Figure 7. The conduction band character and density are consistent with the HSE06 calculation, while the valence band has approximately equal contributions from nickel and oxygen, as opposed to the oxygen-rich character observed in the PBE+U calculation.

The PBE+U band structure of $NiSb_2O_6$ (Figure 8D) reveals that the conduction band edge is highly dispersive. Furthermore, the density of states of $Ni_2Sb_2O_7$ appears to have a very similar band edge character to that of $NiSb_2O_6$ (Figure 8C). Given the similarity of these electronic structures irrespective of Ni:Sb stoichiometry and level of first principles theory, which is corroborated by the similarity of band energetics of am-$NiSbO_z$ and $NiSb_2O_6$ in Figure 7, we hypothesize that Ni-Sb oxides may generally host highly dispersive bands near the conduction band edge, raising the possibility of facile band transport of electrons upon optimization of materials synthesis.

DISCUSSION

It is worth noting that the vast majority of metal oxide photoanodes are based on crystalline phases, while the most effective passivation layers are amorphous due to their lack of crystal anisotropies and defects such as grain boundaries.[53,54] Amorphous semiconductors are normally considered to have poor charge carrier transport due to chemical disorder and low optoelectronic efficiency compared with crystalline semiconductors. Since the discovery of enhanced photocatalysis of so-called black TiO_2,[55] there is a growing interest in exploring amorphous semiconductors for solar cell, photoelectrocatalytic, and photocatalytic applications.[56] For example, varying composition in amorphous metal oxide films to tune band gap and light absorption;[57] exploring amorphous mixed-metal oxides as photocatalysts to enhance water oxidation kinetics;[58] forming crystal-amorphous junction semiconductors to improve charge separation and transportation;[59,60] nano-structuring amorphous materials to increase specific surface and expose more active sites;[61] developing amorphous metal oxide on crystalline semiconductor as a protection layer to prevent corrosion.[62,63] However, there are few reports on amorphous semiconductors used as photoanodes for solar fuel generation.

Amorphous TiO_2 has been shown to exhibit some photoactivity[64] but has been more effectively utilized as a capping layer atop traditional *n*-TiO_2 absorbers. A sol-gel-derived $CuSnO_3$ amorphous thin film with band gap 2.3 eV had a low turn-on/onset potential of 0.3 V versus RHE for OER in pH 6.5, but the photocurrent is unstable with a 50% drop within 25 min.[65] Photoanodes made from amorphous $(Zn, Si)_2GeO_4$ nanowire arrays exhibited a better efficiency and stability in PEC water splitting compared with the crystalline Zn_2GeO_4.[66] In this work, the combinatorial study of photoactivity (Figure 1) reveals that the amorphous material has a higher EQE at and above 2.8 eV than the neighboring composition regions, and perhaps even more striking is that the amorphous photoanode exhibits photoresponse down to a photon energy of approximately 2 eV. Given the chemical and electronic similarities established between am-$NiSbO_z$ and $NiSb_2O_6$, the visible photoresponse of am-$NiSbO_z$ is commensurate with the electronic structure characterization in Figures 7 and 8, where the band diagrams also suggest that the electronic structure of nickel antimonates may generally be conductive to band transport. However, these observations do not reveal why am-$NiSbO_z$ outperforms $NiSb_2O_6$, which can be addressed in future work by disambiguating whether the increased concentration of Ni^{+2} or the lack of crystallinity are most central to photoactivity. Subsequent investigation of the corresponding change in the electronic structure and/or the formation energy and electronic contribution of defects will facilitate understanding of amorphous photoanodes as well as directions for further optimization of am-$NiSbO_z$.

Among amorphous semiconductors, am-$NiSbO_z$ is especially promising due to its thermodynamic Pourbaix stability, as evidenced by the low dissolved metals concentrations under operation, approximately 1 and 20 nmol L^{-1} for Sb and Ni, respectively. Table S6 compares dissolved metals concentrations of am-$NiSbO_z$ with other photoanodes, e.g., WO_3, α-$SnWO_4$, and $BiVO_4$. While dissolved metals concentrations are rarely reported alongside photocatalytic activity and the variation in PEC protocols hinders comparisons among literature reports, we established the comparisons of Table S6 by considering reports from PEC operation at 1.23 V versus RHE for 20–240 min. The PEC stability of photoanodes is strongly pH and electrolyte dependent per the Pourbaix thermodynamics of the respective photocatalyst material. WO_3 is Pourbaix-stable under OER conditions in acid and has enabled operational stability at low pH both as a photoanode and as a self-passivation layer for

α-$SnWO_4$.[25] WO_3 in 0.5 M H_2SO_4 exhibits the lowest dissolved metals concentration observed for these photoanodes (0.87 μmol L^{-1}),[67] which is 40× higher than our measurement of am-$NiSbO_z$ in pH 10 (0.021 μmol L^{-1}). Efforts to mitigate $BiVO_4$ corrosion revealed relatively low dissolution in low-concentration phosphate electrolytes (pH 6.8, 0.1 M KPi).[68] After 60 min operation, the dissolved metals concentrations were negligible for Bi and 0.08 μmol L^{-1} for V, which is 4× higher than that demonstrated by am-$NiSbO_z$ in this work. The low dissolved metals concentration observed in Figure 4B is not only an important demonstration of stability but is also imperative for long-term durability.

Operational stability at any dissolved metals concentration can only be maintained if the dissolved metals remain in the anolyte (the electrolyte in electrochemical communication with the photoanode). For long-term operation, a finite rate of metal precipitation can be expected within the electrolyte, particularly a polymer electrolyte membrane, and/or on the opposing electrode, which has been documented as a prominent device degradation pathway.[69] The flux of dissolved metals from the anolyte will also instigate further corrosion of the photoanode. These considerations highlight the importance of developing photoanodes with favorable Pourbaix energetics, as opposed to dosing the electrolyte with large dissolved metals concentrations. The development of photoanodes that operate with minimal dissolved metals concentration can address the durability challenges of solar fuel generators via codesigned mutual compatibility with other device components.[9]

The combination of computational Pourbaix screening and high-throughput experimentation is particularly well suited for deploying this codesign research strategy, where the former identifies composition systems of interest and the latter identifies the performant materials. In the present case, the performant material is a previously unknown amorphous $NiSbO_z$ photoanode, where z is estimated to be 3.5 corresponding to formal oxidation states of Ni^{+2} and Sb^{+5}. Electrochemical analyses demonstrate that am-$NiSbO_z$ exhibits a promising combination of stability, broad spectral response, and a turn-on potential below 0.4 V versus RHE. The computational Pourbaix stability is mirrored by a very low dissolved metals concentration during operation in pH 10 electrolyte, which is pertinent not only to device-level durability but also to the maintenance of the semiconductor-liquid junction given that operational stability is not reliant on a thick protection layer. The additional inherent lack of crystal anisotropies in this amorphous photoanode opens new opportunities for scalable synthesis. Collectively these results highlight the opportunity for optimizing the photoactivity of am-$NiSbO_z$ and more generally for developing amorphous photoelectrodes to address the activity-durability-scalability challenges in solar fuel generation.

EXPERIMENTAL PROCEDURES

Resource availability

Lead contact

Further information and requests for resources should be directed to the lead contact, John M. Gregoire (gregoire@caltech.edu).

Materials availability

This study did not generate new unique reagents.

Data and code availability

Computational and experimental data are available at https://data.caltech.edu/records/20057 (10.22002/D1.20057). The code for processing experimental data is available at https://github.com/johnmgregoire/JCAPDataProcess.

Physical vapor deposition of $Ni_xSb_{1-x}O_z$ composition library

$Ni_xSb_{1-x}O_z$ composition library was fabricated atop 100-mm-diameter SnO_2:F(FTO)/glass substrate by reactive co-sputtering of Ni and Sb metal sources using 103 and 55 W radio frequency power supplies, respectively, in a custom-designed combinatorial sputtering system.[1] The deposition proceeded at room temperature without intentional heating in a mixed O_2 (0.9 mTorr) and Ar (5.1 mTorr) atmosphere with 10^{-8} Torr base pressure, followed by a post-deposition anneal in a box oven at 610°C in air for 1 h. The non-confocal geometry of sputter sources provided a continuous composition gradient spanning a 60–70 at % range in the concentration of each cation element across the substrate. A duplicate $Ni_xSb_{1-x}O_z$ composition library was fabricated on a 100-mm-diameter Pt/Ti/SiO_2/Si wafer under the same deposition and annealing process.

X-ray fluorescence

The metal oxide compositions were characterized by X-ray fluorescence (XRF) using an EDAX Orbis Micro-XRF system to obtain Ni, Sb metal contents and values of x = Ni/(Ni + Sb) with ca. 1 at % relative uncertainty. The sensitivity factor for Ni and Sb was calibrated by commercial XRF calibration standards (MICROMATTER). The oxygen signal and thus stoichiometry was not detectable by the XRF experiment. Assuming the bulk density of oxides of each element, the XRF measurements also provided an estimate of film thickness.

XRD

The bulk crystal structure and phase distribution of the composition library were determined by XRD using a Bruker DISCOVER D8 diffractometer with Cu Kα radiation from a Bruker Iμs source. The X-ray spot size was limited to a 2 mm length scale, over which the composition was constant within approximately 1–2 at %. Diffraction images were collected using a two-dimensional VÅNTEC-500 detector and integrated into one-dimensional patterns using DIFFRAC.SUITE EVA software. The crystal structures present in each sample were identified by matching the XRD patterns with entries in the International Crystallography Diffraction Database in the EVA.

XPS

XPS spectra were measured to determine the near-surface chemistry using a Kratos Axis Ultra Nova instrument with a base pressure $<10^{-9}$ Torr. A monochromatic Al Kα (1,486.6 eV) source with a power of 150 W was used for all wide, valence band, and core-level detail scans, whereas 10 W was used for work function measurements. The collected spectra were calibrated to the carbon 1s peak of 284.8 eV. Data were analyzed using CasaXPS. The valence band edge is the region close to zero binding energy (maximum kinetic energy). The VBM was determined by the intersection of a linear fit to the background and the onset of the valence band. The work function of the sample was determined by measuring the secondary electron cutoff of the sample while biasing the sample with a stabilized voltage source (+40 V) to overcome the work function of the analyzer. The spectra were then corrected by the applied bias, and the position of the secondary electron cutoff edge was determined by the interception of a linear fit to the edge. In an intensity versus kinetic energy plot, this value at the intersection will directly yield the value of the work function. For the binding energy scale, the value must be converted by the photon energy. A Shirley background model was applied to quantify the core-level intensities, which were corrected by the analyzer transmission function and relative sensitivity factors to obtain corrected peak intensities and atomic ratios.

XAS

XAS at Ni K-edge (8,333 eV) and Sb K-edge (30,491 eV) were measured at beamline 7-3 of Stanford Synchrotron Radiation Lightsource ([SLAC], CA, USA). The intensity of the incident X-rays was monitored using an Ar-filled ion chamber (Sb K-edge) and an N_2-filled ion chamber (Ni K-edge). The Ni_xSb_{1-x} samples were measured in fluorescence mode using a 30-element Ge detector (Canberra). An Sb foil and a Ni foil were used for XAS energy calibration. The first inflexion point of the Ni foil spectrum and Sb foil spectrum were calibrated to 8,333.0 and 30,491.0 eV. The data for Ni_xSb_{1-x} was recorded in continuous scan mode. The XAS data reduction was carried out with the SamView program included in the SixPack software package (http://www.sams-xrays.com/sixpack), and the data processing and analysis were performed with Athena software, Demeter version 0.9.26.[70]

UV-vis spectroscopy

The optical properties of the composition libraries were characterized using a custom-built on-the-fly scanning UV-vis dual-sphere spectrometer to record transmittance (T) and total reflectance (R) simultaneously.[2] The fractional T and R spectra were used to calculate the spectral absorption coefficient (α) as $\alpha = -\ln[T*(1-R)^{-1}]/\tau$, where τ is film thickness. The optical spectra were acquired on a 2-mm-grid of 1,521 positions on the composition library and automatically processed for Tauc analysis.[3]

TEM and EDX

TEM experiments were carried out in an FEI Tecnai Osiris FEG/TEM operated at 200 kV in bright-field and high-resolution TEM mode. SAED patterns were taken using the same machine. EDX elemental mapping was acquired using Bruker Quantax. This characterization was performed using a Eurofins EAG Precision TEM in Santa Clara, CA.

Mobility measurements

Electronic transport measurements were performed in a van der Pauw geometry. Linear regression fitting of current-voltage sweeps collected between all adjacent contacts resulted in a minimum R^2 value of 0.9999, confirming ohmic contacts. The final excitation current of 10 μA chosen for Hall analysis was within this ohmic range. Hall effect measurements employed the FastHall approach using a LakeShore cryotronics probe station equipped with a 1 Tesla permanent magnet. This method is more amenable to low mobility films than conventional DC Hall effect measurements. In the 100 measurements performed, the Hall voltage was found to be negative 90 times. To further verify the measurement's reliability, the field was intentionally reversed and, in this case, we measured an equal-but-opposite signal (similar mobility, but majority positive voltages).

Photoelectrochemistry

Combinatorial PEC measurements were conducted in our previously reported fiber-coupled SDC instrumentation with a Gamry G 300 potentiostat controlled by custom automation software.[4] Experiments were carried out in three 1 atm O_2-saturated aqueous electrolytes (see Table S1) with a sacrificial hole acceptor to increase the hole transfer kinetics at the film/electrolyte interface. The Doric LEDs with four different photon energies (2.06, 2.4, 2.7, and 3.2 eV) were used as the front-side toggled illumination source and the power of each LED is listed in Tables S2 and S3. At each sample, four sequential CA were measured at 1.23 V versus RHE with four LEDs toggled with 0.5 s on/off illumination: 3.2 eV for 15 s and 2.7, 2.4, and

2.06 eV all for 4 s each, immediately followed by cyclic voltammetry (CV) from 1.23 to 0.73 and back to 1.53 V versus RHE (rate of 0.02 V s^{-1}) under the 3.2 eV illumination with light toggling 1.33 s on and 0.67 s off. Spectral EQE (also called incident photon-to-current efficiency) was calculated to investigate the relationship between the PEC activity and the incident photon energy.

Selected x = 0.5 composition photoanodes were evaluated for their PEC stability with respect to the applied potentials in all three electrolytes: MET1, SLF7, and SLF10. In each electrolyte, a series of CV sweeps under 3.2 eV chopped illumination were performed on a fresh clean sample, then followed by a 30 min CA at 1.23 V versus RHE. The first CV scanned a voltage range of 1.23–0.73 V versus RHE, and then each CV thereafter was scanned further down of 0.1 V versus RHE until the onset of dark current.

Further evaluation of operational PEC stability of the $Ni_{0.5}Sb_{0.5}$ photoanode was performed by operating a larger sample (geometric working electrode area of 0.312 cm^2 defined by the o-ring) in a customized fast flow cell (flow rate of 160 μL s^{-1}) coupled with front-side 3.2 eV illumination.[5] Throughout 30 min chopped illumination (290 s on/10 s off) CA at 1.23 V versus RHE in aqueous O_2-bubbled pH 10 electrolyte (74 mL) without the hole acceptor, aliquots of electrolyte (5 mL) at various time points were extracted to quantify the dissolved metal concentrations via ICP-MS.

ICP-MS

ICP-MS using a Thermo Fisher Scientific iCAP RQ instrument was used to determine the concentration of dissolved Ni and Sb metals in the electrolyte used for electrochemistry at different durations throughout the PEC measurement.

Pourbaix calculations

Energetics of the Ni-Sb-O phases were obtained from the Materials Project Database.[71] The Pourbaix diagram was generated using the Pourbaix module in Pymatgen.[26,72]

DFT calculations

First principles DFT calculations were performed with a plane-wave basis and projector-augmented wave potentials[73] using the VASP.[47,48] These calculations were performed in the generalized gradient approximation as implemented by Perdew, Burke, and Ernzerhof (PBE)[49] using additional Hubbard U correction terms in the formalism developed by Dudarev (PBE+U)[50] to account approximately for on-site correlation. A U value of 6.2 eV was used for the Ni ions, consistent with the standard Hubbard U values used in the MP. The plane wave energy cutoff was 600 eV. A 6 × 6 × 2 k grid was used for $NiSb_2O_6$ and a 6 × 6 × 6 k grid was used for $Ni_2Sb_2O_7$. Three collinear magnetic orderings for the Ni ions were considered for both materials, FM ordering and two AFM orderings each. For $NiSb_2O_6$ the Ni octahedra are not connected. Planes of disconnected Ni octahedra in the ab plane are layered with each plane offset by half a lattice parameter, making triangles with an in-plane separation of ~4.7 Å and out-of-plane separations ~5.7 Å apart. The most stable AFM ordering had FM ordering in-plane and AFM ordering between neighboring planes. For $Ni_2Sb_2O_7$ the magnetic ordering is substantially more complex, as previous experimental evidence indicates that this material is a frustrated antiferromagnet.[53] Investigation of various non-collinear magnetic orderings would be more appropriate for identifying the ground-state magnetic ordering of $Ni_2Sb_2O_7$, but that is beyond the scope of this work. Ni sites are clustered in groups

of four with edge-sharing polyhedra and the lowest energy collinear AFM magnetic ordering investigated consisted of two of the polyhedra in each cluster with parallel magnetic moments and the other two with their magnetic moments in the opposite direction. Structural relaxations were performed for both materials for both FM and AFM collinear magnetic orderings with forces converged to <0.001 eV/Å. The density of states and band structure calculations were performed for both $NiSb_2O_6$ and $Ni_2Sb_2O_7$ using PBE+U with 10 × 10 × 2 and 10 × 10 × 10 k-point grids, respectively. The density of states of $NiSb_2O_6$ was also calculated using HSE06[51,52] with an energy cutoff of 500 eV, a 6 × 6 × 2 k-point grid, and the structure obtained from relaxation with PBE+U.

SUPPLEMENTAL INFORMATION

Supplemental information can be found online at https://doi.org/10.1016/j.xcrp.2022.100959.

ACKNOWLEDGMENTS

This material is based on work performed by the Liquid Sunlight Alliance, which is supported by the US Department of Energy, Office of Science, Office of Basic Energy Sciences, Fuels from Sunlight Hub under award DE-SC0021266. This research used computing resources from the Lawrencium computational cluster resource provided by the IT Division at the Lawrence Berkeley National Laboratory, supported by the Director, Office of Science, Office of Basic Energy Sciences, of the US Department of Energy under contract no. DE-AC02-05CH11231. Use of the Stanford Synchrotron Radiation Lightsource (beamlines 7-3 and 9-3), SLAC National Accelerator Laboratory, is supported by the US Department of Energy, Office of Science, Office of Basic Energy Sciences under contract no. DE-AC02-76SF00515. National Renewable Energy Laboratory is operated by the Alliance for Sustainable Energy, LLC, for the US Department of Energy (DOE) under contract no. DE-AC36-08GO28308. The Resnick Sustainability Institute at Caltech is also acknowledged for its support of enabling infrastructure and facilities. The views expressed in this article do not necessarily represent the views of the DOE or the US Government.

AUTHOR CONTRIBUTIONS

L.Z. conducted synthesis and diffraction experiments with support from K.K. Electronic structure calculations were conducted by E.A.P. and J.B.N. The grand potential and Pourbaix phase diagrams were created by K.K.R. and M.B. Photoelectrochemistry experiments were conducted by Y.L. and Y.W. Optical spectroscopy measurements were conducted by P.F.N. X-ray absorption measurements were conducted by X.L. and analyzed by Y.L. under guidance from J.Y. Electronic structure experiments were conducted by M.H.R. Hall measurements were conducted by S.R.B. J.M.G. supervised the work, designed experiments, and coordinated manuscript writing along with L.Z. using contributions from all authors.

DECLARATION OF INTERESTS

The authors declare no competing interests.

Received: March 23, 2022
Revised: May 27, 2022
Accepted: June 8, 2022
Published: June 27, 2022

REFERENCES

1. Walter, M.G., Warren, E.L., McKone, J.R., Boettcher, S.W., Mi, Q., Santori, E.A., and Lewis, N.S. (2010). Solar water splitting cells. Chem. Rev. *110*, 6446–6473. https://doi.org/10.1021/cr1002326.

2. Hu, S., Xiang, C., Haussener, S., Berger, A.D., and Lewis, N.S. (2013). An analysis of the optimal band gaps of light absorbers in integrated tandem photoelectrochemical water-splitting systems. Energy Environ. Sci. *6*, 2984–2993. https://doi.org/10.1039/C3EE40453F.

3. Fountaine, K.T., Lewerenz, H.J., and Atwater, H.A. (2016). Efficiency limits for photoelectrochemical water-splitting. Nat. Commun. *7*, 13706. https://doi.org/10.1038/ncomms13706.

4. DOE Technical Targets for Hydrogen Production from Photoelectrochemical Water Splitting. Energy.gov. https://www.energy.gov/eere/fuelcells/doe-technical-targets-hydrogen-production-photoelectrochemical-water-splitting.

5. Lee, D.K., Lee, D., Lumley, M.A., and Choi, K.-S. (2019). Progress on ternary oxide-based photoanodes for Use in photoelectrochemical cells for solar water splitting. Chem. Soc. Rev. *48*, 2126–2157. https://doi.org/10.1039/C8CS00761F.

6. Abdi, F.F., and Berglund, S.P. (2017). Recent developments in complex metal oxide photoelectrodes. J. Phys. Appl. Phys. *50*, 193002. https://doi.org/10.1088/1361-6463/aa6738.

7. Xiao, M., Luo, B., Wang, Z., Wang, S., and Wang, L. (2020). Recent advances of metal-oxide photoanodes: engineering of charge separation and transportation toward efficient solar water splitting. Solar RRL *4*, 1900509. https://doi.org/10.1002/solr.201900509.

8. He, H., Liao, A., Guo, W., Luo, W., Zhou, Y., and Zou, Z. (2019). State-of-the-Art progress in the Use of ternary metal oxides as photoelectrode materials for water splitting and organic synthesis. Nano Today *28*, 100763. https://doi.org/10.1016/j.nantod.2019.100763.

9. Rao, K.K., Lai, Y., Zhou, L., Haber, J.A., Bajdich, M., and Gregoire, J.M. (2022). Overcoming hurdles in oxygen evolution catalyst discovery via codesign. Chem. Mater. *34*, 899–910. https://doi.org/10.1021/acs.chemmater.1c04120.

10. Yan, Q., Yu, J., Suram, S.K., Zhou, L., Shinde, A., Newhouse, P.F., Chen, W., Li, G., Persson, K.A., Gregoire, J.M., and Neaton, J.B. (2017). Solar fuels photoanode materials discovery by integrating high-throughput theory and experiment. Proc. Natl. Acad. Sci. USA *114*, 3040–3043. https://doi.org/10.1073/pnas.1619940114.

11. Shinde, A., Suram, S.K., Yan, Q., Zhou, L., Singh, A.K., Yu, J., Persson, K.A., Neaton, J.B., and Gregoire, J.M. (2017). Discovery of manganese-based solar fuel photoanodes via integration of electronic structure calculations, Pourbaix stability modeling, and high-throughput experiments. ACS En. Lett. *2*, 2307–2312. https://doi.org/10.1021/acsenergylett.7b00607.

12. Zhou, L., Shinde, A., Guevarra, D., Haber, J.A., Persson, K.A., Neaton, J.B., and Gregoire, J.M. (2020). Successes and opportunities for discovery of metal oxide photoanodes for solar fuels generators. ACS Energy Lett. *5*, 1413–1421. https://doi.org/10.1021/acsenergylett.0c00067.

13. Woodhouse, M., Herman, G.S., and Parkinson, B.A. (2005). Combinatorial approach to identification of catalysts for the photoelectrolysis of water. Chem. Mater. *17*, 4318–4324. https://doi.org/10.1021/cm050546q.

14. Kumari, S., Junqueira, J.R.C., Schuhmann, W., and Ludwig, A. (2020). High-throughput exploration of metal vanadate thin-film systems (M–V–O, M = Cu, Ag, W, Cr, Co, Fe) for solar water splitting: composition, structure, stability, and photoelectrochemical properties. ACS Comb. Sci. *22*, 844–857. https://doi.org/10.1021/acscombsci.0c00150.

15. Gutkowski, R., Khare, C., Conzuelo, F., Kayran, Y.U., Ludwig, A., Ludwig, A., and Schuhmann, W. (2017). Unraveling compositional effects on the light-induced oxygen evolution in Bi(V–Mo–X)O 4 material libraries. Energy Environ. Sci. *10*, 1213–1221. https://doi.org/10.1039/C7EE00287D.

16. Sliozberg, K., Stein, H.S., Khare, C., Parkinson, B.A., Ludwig, A., and Schuhmann, W. (2015). Fe–Cr–Al containing oxide semiconductors as potential solar water-splitting materials. ACS Appl. Mater. Interfaces *7*, 4883–4889. https://doi.org/10.1021/am508946e.

17. Seabold, J.A., and Neale, N.R. (2015). All first row transition metal oxide photoanode for water splitting based on Cu3V2O8. Chem. Mater. *27*, 1005–1013. https://doi.org/10.1021/cm504327f.

18. Guo, W., Chemelewski, W.D., Mabayoje, O., Xiao, P., Zhang, Y., and Mullins, C.B. (2015). Synthesis and characterization of CuV 2 O 6 and Cu 2 V 2 O 7 : two photoanode candidates for photoelectrochemical water oxidation. J. Phys. Chem. C *119*, 27220–27227. https://doi.org/10.1021/acs.jpcc.5b07219.

19. Zhou, L., Yan, Q., Shinde, A., Guevarra, D., Newhouse, P.F., Becerra-Stasiewicz, N., Chatman, S.M., Haber, J.A., Neaton, J.B., and Gregoire, J.M. (2015). High throughput discovery of solar fuels photoanodes in the CuO-V 2 O 5 system. Adv. En. Mater. *5*, 1500968. https://doi.org/10.1002/aenm.201500968.

20. Zhou, L., Yan, Q., Yu, J., Jones, R.J.R., Becerra-Stasiewicz, N., Suram, S.K., Shinde, A., Guevarra, D., Neaton, J.B., Persson, K.A., and Gregoire, J.M. (2016). Stability and self-passivation of copper vanadate photoanodes under chemical, electrochemical, and photoelectrochemical operation. Phys. Chem. Chem. Phys. *18*, 9349–9352. https://doi.org/10.1039/C6CP00473C.

21. Jiang, C.-M., Segev, G., Hess, L.H., Liu, G., Zaborski, G., Toma, F.M., Cooper, J.K., and Sharp, I.D. (2018). Composition-dependent functionality of copper vanadate photoanodes. ACS Appl. Mater. Interfaces *10*, 10627–10633. https://doi.org/10.1021/acsami.8b02977.

22. Wiktor, J., Reshetnyak, I., Strach, M., Scarongella, M., Buonsanti, R., and Pasquarello, A. (2018). Sizable excitonic effects Undermining the photocatalytic efficiency of β-Cu2V2O7. J. Phys. Chem. Lett. *9*, 5698–5703. https://doi.org/10.1021/acs.jpclett.8b02323.

23. Tian, C.M., Jiang, M., Tang, D., Qiao, L., Xiao, H.Y., Oropeza, F.E., Hofmann, J.P., Hensen, E.J.M., Tadich, A., Li, W., et al. (2019). Elucidating the electronic structure of CuWO4 thin films for enhanced photoelectrochemical water splitting. J. Mater. Chem. *7*, 11895–11907. https://doi.org/10.1039/C8TA12070F.

24. Kölbach, M., Hempel, H., Harbauer, K., Schleuning, M., Petsiuk, A., Höflich, K., Deinhart, V., Friedrich, D., Eichberger, R., Abdi, F.F., and van de Krol, R. (2020). Grain boundaries limit the charge carrier transport in pulsed laser deposited α-SnWO4 thin film photoabsorbers. ACS Appl. Energy Mater. *3*, 4320–4330. https://doi.org/10.1021/acsaem.0c00028.

25. Schnell, P., Dela Cruz, J.M.C., Kölbach, M., van de Krol, R., and Abdi, F.F. (2022). PH-dependent stability of α-SnWO4 photoelectrodes. Chem. Mater. *34*, 1590–1598. https://doi.org/10.1021/acs.chemmater.1c03517.

26. Singh, A.K., Zhou, L., Shinde, A., Suram, S.K., Montoya, J.H., Winston, D., Gregoire, J.M., and Persson, K.A. (2017). Electrochemical stability of metastable materials. Chem. Mater. *29*, 10159–10167. https://doi.org/10.1021/acs.chemmater.7b03980.

27. Chen, S., and Wang, L.-W. (2012). Thermodynamic oxidation and reduction potentials of photocatalytic semiconductors in aqueous solution. Chem. Mater. *24*, 3659–3666. https://doi.org/10.1021/cm302533s.

28. Lee, D.K., and Choi, K.-S. (2018). Enhancing long-term photostability of BiVO4 photoanodes for solar water splitting by tuning electrolyte composition. Nat. Energy *3*, 53–60. https://doi.org/10.1038/s41560-017-0057-0.

29. Cassidy, T.J., Pollastri, M., and Trifirò, F. (1997). Ammoxidation of propane on nickel antimonates. J. Catal. *172*, 55–63. https://doi.org/10.1006/jcat.1997.1865.

30. Singh, A., Singh, A., Singh, S., and Tandon, P. (2016). Nickel antimony oxide (NiSb2O6): a fascinating nanostructured material for gas sensing application. Chem. Phys. Lett. *646*, 41–46. https://doi.org/10.1016/j.cplett.2016.01.005.

31. Guillén Bonilla, A., Rodríguez Betancourtt, V.M., Guillén Bonilla, H., Gildo Ortiz, L., Blanco Alonso, O., Franco Rodríguez, N.E., Reyes Gómez, J., Casillas Zamora, A., and Guillen Bonilla, J.T. (2018). A new CO2 detection system based on the trirutile-type CoSb2O6 oxide. J. Mater. Sci. Mater. Electron. *29*, 15741–15753. https://doi.org/10.1007/s10854-018-9228-4.

32. Casillas-Zamora, A., Guillén-Bonilla, J.T., Guillén-Bonilla, A., Rodríguez-Betancourtt, M., Casallas-Moreno, Y.L., Gildo-Ortiz, L., de la Luz Olvera-Amador, M., Tomás, S.A., and Guillén-Bonilla, H. (2020). Synthesis of MnSb2O6 powders through a simple low-temperature

method and their test as a gas sensor. J. Mater. Sci. Mater. Electron. *31*, 7359–7372. https://doi.org/10.1007/s10854-019-02700-3.

33. Han, J., Xu, M., Jia, M., and Liu, T. (2016). Evaluation of reduced graphene oxide-supported NiSb2O6 nanocomposites for reversible lithium storage. Ceram. Int. *42*, 14782–14787. https://doi.org/10.1016/j.ceramint.2016.06.108.

34. Arunkumar, N., and Naraginti, S. (2020). Facile synthesis of nanostructured trirutile antimonates M(II)Sb2O6 (M = Co, Cu, Ni, Fe) and its visible photocatalytic studies. Inorg. Nano-Met. Chem. *0*, 1–10. https://doi.org/10.1080/24701556.2020.1866605.

35. Papi, N., Hakimyfard, A., Tahmasebi, N., and Samimifar, M. (2020). Photocatalytic degradation of water pollutant dye by solid state synthesized Ni1-XLnxSb2O6 (Ln=Eu, Gd, Ho and Yb) nanocomposites. Int. J. Nano Dimens. *11*, 377–391.

36. Wang, Z., Zheng, Y.-R., Chorkendorff, I., and Nørskov, J.K. (2020). Acid-stable oxides for oxygen electrocatalysis. ACS Energy Lett. *5*, 2905–2908. https://doi.org/10.1021/acsenergylett.0c01625.

37. Gunasooriya, G.T.K., and Nørskov, J.K. (2020). Analysis of acid-stable and active oxides for the oxygen evolution reaction. ACS Energy Lett. *5*, 3778–3787. https://doi.org/10.1021/acsenergylett.0c02030.

38. Moreno-Hernandez, I.A., MacFarland, C.A., Read, C.G., Papadantonakis, K.M., Brunschwig, B.S., and Lewis, N.S. (2017). Crystalline nickel manganese antimonate as a stable water-oxidation catalyst in aqueous 1.0 M H_2SO_4. Energy Environ. Sci. *10*, 2103–2108. https://doi.org/10.1039/C7EE01486D.

39. Zhou, L., Shinde, A., Montoya, J.H., Singh, A., Gul, S., Yano, J., Ye, Y., Crumlin, E.J., Richter, M.H., Cooper, J.K., et al. (2018). Rutile alloys in the Mn–Sb–O system stabilize Mn3+ to enable oxygen evolution in strong acid. ACS Catal. *8*, 10938–10948. https://doi.org/10.1021/acscatal.8b02689.

40. Evans, T.A., and Choi, K.-S. (2020). Electrochemical synthesis and investigation of stoichiometric, phase-pure CoSb2O6 and MnSb2O6 electrodes for the oxygen evolution reaction in acidic media. ACS Appl. Energy Mater. *3*, 5563–5571. https://doi.org/10.1021/acsaem.0c00526.

41. Ham, K., Hong, S., Kang, S., Cho, K., and Lee, J. (2021). Extensive active-site formation in trirutile CoSb2O6 by oxygen vacancy for oxygen evolution reaction in anion exchange membrane water splitting. ACS Energy Lett. *6*, 364–370. https://doi.org/10.1021/acsenergylett.0c02359.

42. Moreno-Hernandez, I.A., Brunschwig, B.S., and Lewis, N.S. (2019). Crystalline nickel, cobalt, and manganese antimonates as electrocatalysts for the chlorine evolution reaction. Energy Environ. Sci. *12*, 1241–1248. https://doi.org/10.1039/C8EE03676D.

43. Zhou, L., Li, H., Lai, Y., Richter, M., Kan, K., Haber, J.A., Kelly, S., Wang, Z., Lu, Y., Kim, R.S., et al. (2022). Stability and activity of cobalt antimonate for oxygen reduction in strong acid. ACS Energy Lett. *7*, 993–1000. https://doi.org/10.1021/acsenergylett.1c02673.

44. Gunasooriya, G.T.K., Kreider, M.E., Liu, Y., Zamora Zeledón, J.A., Wang, Z., Valle, E., Yang, A.-C., Gallo, A., Sinclair, R., Stevens, M.B., et al. (2022). First-row transition metal antimonates for the oxygen reduction reaction. ACS Nano *16*, 6334–6348. https://doi.org/10.1021/acsnano.2c00420.

45. Zhou, H.D., Wiebe, C.R., Janik, J.A., Vogt, B., Harter, A., Dalal, N.S., and Gardner, J.S. (2010). Spin glass transitions in the absence of chemical disorder for the pyrochlores A2Sb2O7 (A=Mn, Co, Ni). J. Solid State Chem. *183*, 890–894. https://doi.org/10.1016/j.jssc.2010.01.025.

46. Rettie, A.J.E., Lee, H.C., Marshall, L.G., Lin, J.-F., Capan, C., Lindemuth, J., McCloy, J.S., Zhou, J., Bard, A.J., and Mullins, C.B. (2013). Combined charge carrier transport and photoelectrochemical characterization of BiVO4 single crystals: intrinsic behavior of a complex metal oxide. J. Am. Chem. Soc. *135*, 11389–11396. https://doi.org/10.1021/ja405550k.

47. Kresse, G., and Furthmüller, J. (1996). Efficiency of ab-initio total energy calculations for metals and semiconductors using a plane-wave basis set. Comput. Mater. Sci. *6*, 15–50. https://doi.org/10.1016/0927-0256(96)00008-0.

48. Kresse, G., and Furthmüller, J. (1996). Efficient iterative schemes for ab initio total-energy calculations using a plane-wave basis set. Phys. Rev. B *54*, 11169–11186. https://doi.org/10.1103/PhysRevB.54.11169.

49. Perdew, J.P., Burke, K., and Ernzerhof, M. (1996). Generalized gradient approximation made simple. Phys. Rev. Lett. *77*, 3865–3868. https://doi.org/10.1103/PhysRevLett.77.3865.

50. Dudarev, S.L., Botton, G.A., Savrasov, S.Y., Humphreys, C.J., and Sutton, A.P. (1998). Electron-energy-loss spectra and the structural stability of nickel oxide: an LSDA+U study. Phys. Rev. B *57*, 1505–1509. https://doi.org/10.1103/PhysRevB.57.1505.

51. Heyd, J., Scuseria, G.E., and Ernzerhof, M. (2003). Hybrid functionals based on a screened coulomb potential. J. Chem. Phys. *118*, 8207–8215. https://doi.org/10.1063/1.1564060.

52. Krukau, A.V., Vydrov, O.A., Izmaylov, A.F., and Scuseria, G.E. (2006). Influence of the exchange screening parameter on the performance of screened hybrid functionals. J. Chem. Phys. *125*, 224106. https://doi.org/10.1063/1.2404663.

53. Aykol, M., and Persson, K.A. (2018). Oxidation protection with amorphous surface oxides: thermodynamic insights from ab initio simulations on aluminum. ACS Appl. Mater. Interfaces *10*, 3039–3045. https://doi.org/10.1021/acsami.7b14868.

54. Revesz, A.G., and Fehlner, F.P. (1981). The role of noncrystalline films in the oxidation and corrosion of metals. Oxid. Met. *15*, 297–321. https://doi.org/10.1007/BF01058831.

55. Chen, X., Liu, L., Yu, P.Y., and Mao, S.S. (2011). Increasing solar absorption for photocatalysis with black hydrogenated titanium dioxide nanocrystals. Science *331*, 746–750. https://doi.org/10.1126/science.1200448.

56. Wang, B., Biesold, G.M., Zhang, M., and Lin, Z. (2021). Amorphous inorganic semiconductors for the development of solar cell, photoelectrocatalytic and photocatalytic applications. Chem. Soc. Rev. *50*, 6914–6949. https://doi.org/10.1039/D0CS01134G.

57. Chen, L., Shet, S., Tang, H., Ahn, K.s., Wang, H., Yan, Y., Turner, J., and Al-Jassim, M. (2010). Amorphous copper tungsten oxide with tunable band gaps. J. Appl. Phys. *108*, 043502. https://doi.org/10.1063/1.3475714.

58. Smith, R.D.L., Prévot, M.S., Fagan, R.D., Zhang, Z., Sedach, P.A., Siu, M.K.J., Trudel, S., and Berlinguette, C.P. (2013). Photochemical route for accessing amorphous metal oxide materials for water oxidation catalysis. Science *340*, 60–63. https://doi.org/10.1126/science.1233638.

59. Choi, H., Han, H., Moon, S.-I., Je, M., Lee, S., Kwon, J., Kim, S., Lee, K.-R., Ali, G., Mathur, S., et al. (2022). Strategy to utilize amorphous phase of semiconductor toward excellent and reliable photochemical water splitting performance: roles of interface dipole moment and reaction parallelization. Int. J. Energy Res. *46*, 3674–3685. https://doi.org/10.1002/er.7333.

60. Liu, W., Liu, H., Dang, L., Zhang, H., Wu, X., Yang, B., Li, Z., Zhang, X., Lei, L., and Jin, S. (2017). Amorphous cobalt–iron hydroxide nanosheet electrocatalyst for efficient electrochemical and photo-electrochemical oxygen evolution. Adv. Funct. Mater. *27*, 1603904. https://doi.org/10.1002/adfm.201603904.

61. Zhao, W., Xu, T., Li, T., Wang, Y., Liu, H., Feng, J., Ding, S., Li, Z., and Wu, M. (2018). Amorphous iron(III)-Borate nanolattices as multifunctional electrodes for self-driven overall water splitting and rechargeable zinc–air battery. Small *14*, 1802829. https://doi.org/10.1002/smll.201802829.

62. Verlage, E., Hu, S., Liu, R., Jones, R.J.R., Sun, K., Xiang, C., Lewis, N.S., and Atwater, H.A. (2015). A monolithically integrated, intrinsically safe, 10% efficient, solar-driven water-splitting system based on active, stable earth-abundant electrocatalysts in conjunction with tandem III–V light absorbers protected by amorphous TiO2 films. Energy Environ. Sci. *8*, 3166–3172. https://doi.org/10.1039/C5EE01786F.

63. Hu, S., Shaner, M.R., Beardslee, J.A., Lichterman, M., Brunschwig, B.S., and Lewis, N.S. (2014). Amorphous TiO2 coatings stabilize Si, GaAs, and GaP photoanodes for efficient water oxidation. Science *344*, 1005–1009. https://doi.org/10.1126/science.1251428.

64. Liang, J., Wang, N., Zhang, Q., Liu, B., Kong, X., Wei, C., Zhang, D., Yan, B., Zhao, Y., and Zhang, X. (2017). Exploring the mechanism of a pure and amorphous black-blue TiO2:H thin film as a photoanode in water splitting. Nano Energy *42*, 151–156. https://doi.org/10.1016/j.nanoen.2017.10.062.

65. Kim, B.N., Seo, G.K., Hwang, S.W., Yu, H., Ahn, B., Seo, H., and Cho, I.S. (2018). Photophysical properties and photoelectrochemical performances of sol-gel derived copper stannate (CuSnO3) amorphous semiconductor for solar water splitting application. Ceram. Int. *44*, 1843–1849. https://doi.org/10.1016/j.ceramint.2017.10.119.

66. He, T., Zu, L., Zhang, Y., Mao, C., Xu, X., Yang, J., and Yang, S. (2016). Amorphous semiconductor nanowires created by site-specific heteroatom substitution with significantly enhanced photoelectrochemical performance. ACS Nano *10*, 7882–7891. https://doi.org/10.1021/acsnano.6b03801.

67. Le, H.V., Pham, P.T., Le, L.T., Nguyen, A.D., Tran, N.Q., and Tran, P.D. (2021). Fabrication of tungsten oxide photoanode by doctor blade technique and investigation on its photocatalytic operation mechanism. Int. J. Hydrogen Energy *46*, 22852–22863. https://doi.org/10.1016/j.ijhydene.2021.04.113.

68. Toma, F.M., Cooper, J.K., Kunzelmann, V., McDowell, M.T., Yu, J., Larson, D.M., Borys, N.J., Abelyan, C., Beeman, J.W., Yu, K.M., et al. (2016). Mechanistic insights into chemical and photochemical transformations of bismuth vanadate photoanodes. Nat. Commun. *7*, 12012. https://doi.org/10.1038/ncomms12012.

69. Haraldsted, J.-P.B., Révay, Z., Frydendal, R., Verdaguer-Casadevall, A., Rossmeisl, J., Kibsgaard, J., and Chorkendorff, I. (2019). Trace anodic migration of iridium and titanium ions and subsequent cathodic selectivity degradation in acid electrolysis systems. Mater. Today Energy *14*, 100352. https://doi.org/10.1016/j.mtener.2019.100352.

70. Ravel, B., and Newville, M. (2005). *ATHENA*, *ARTEMIS*, *HEPHAESTUS*: data analysis for X-ray absorption spectroscopy using*IFEFFIT*. J. Synchrotron Radiat. *12*, 537–541. https://doi.org/10.1107/S0909049505012719.

71. Jain, A., Ong, S.P., Hautier, G., Chen, W., Richards, W.D., Dacek, S., Cholia, S., Gunter, D., Skinner, D., Ceder, G., and Persson, K.A. (2013). Commentary: the materials Project: a materials genome approach to accelerating materials innovation. Apl. Mater. *1*, 011002. https://doi.org/10.1063/1.4812323.

72. Persson, K.A., Waldwick, B., Lazic, P., and Ceder, G. (2012). Prediction of solid-aqueous equilibria: scheme to combine first-principles calculations of solids with experimental aqueous states. Phys. Rev. B *85*, 235438. https://doi.org/10.1103/PhysRevB.85.235438.

73. Kresse, G., and Joubert, D. (1999). From Ultrasoft pseudopotentials to the projector augmented-wave method. Phys. Rev. B *59*, 1758–1775. https://doi.org/10.1103/PhysRevB.59.1758.